



# Complex patterns of subcellular cardiac alternans

Joshua Veasy, Yi Ming Lai, Stephen Coombes, Rüdiger Thul\*

Centre for Mathematical Medicine and Biology, School of Mathematical Sciences, University of Nottingham, Nottingham NG7 2RD, UK

## ARTICLE INFO

### Article history:

Received 4 February 2019

Revised 12 June 2019

Accepted 16 June 2019

Available online xxx

### Keywords:

Intracellular calcium dynamics

Network dynamics

Synchrony

Cytosolic and luminal calcium diffusion

## ABSTRACT

Cardiac alternans, in which the membrane potential and the intracellular calcium concentration exhibit alternating durations and peak amplitudes at consecutive beats, constitute a precursor to fatal cardiac arrhythmia such as sudden cardiac death. A crucial question therefore concerns the onset of cardiac alternans. Typically, alternans are only reported when they are fully developed. Here, we present a modelling approach to explore recently discovered microscopic alternans, which represent one of the earliest manifestations of cardiac alternans. In this case, the regular periodic dynamics of the local intracellular calcium concentration is already unstable, while the whole-cell behaviour suggests a healthy cell state. In particular, we use our model to investigate the impact of calcium diffusion in both the cytosol and the sarcoplasmic reticulum on the formation of microscopic calcium alternans. We find that for dominant cytosolic coupling, calcium alternans emerge via the traditional period doubling bifurcation. In contrast, dominant luminal coupling leads to a novel route to calcium alternans through a saddle-node bifurcation at the network level. Combining semi-analytical and computational approaches, we compute areas of stability in parameter space and find that as we cross from stable to unstable regions, the emergent patterns of the intracellular calcium concentration change abruptly in a fashion that is highly dependent upon position along the stability boundary. Our results demonstrate that microscopic calcium alternans may possess a much richer dynamical repertoire than previously thought and further strengthen the role of luminal calcium in shaping cardiac calcium dynamics.

© 2019 The Authors. Published by Elsevier Ltd.

This is an open access article under the CC BY license. (<http://creativecommons.org/licenses/by/4.0/>)

## 1. Introduction

Cardiac arrhythmias progress through a number of stages before becoming life-threatening. One of the earliest indications of a pathological condition are T-wave alternans in the electrocardiogram (ECG) (Qu et al., 2010; 2014). Here, the amplitude of the T-wave in the ECG alternates between large and small values on successive heartbeats. There is now compelling evidence that these macroscopic signals emerge from pathologies at the single cell level. Indeed, alternations in the action potential duration (APD) and the intracellular calcium ( $\text{Ca}^{2+}$ ) concentration have been firmly linked with T-wave alternans (Qu et al., 2010; 2014). Consequentially, single cell alternans have received substantial attention (Alvarez-Lacalle et al., 2015; Weiss et al., 2006; Shiferaw et al., 2003; Cherry, 2017; Tomek et al., 2018; Alvarez-Lacalle et al., 2013; Groenendaal et al., 2014; Shiferaw et al., 2005; Restrepo et al., 2008; Kanaporis and Blatter, 2017; Edwards and Blatter, 2014; Shkryl et al., 2012; Qu et al., 2016).

A significant milestone in the study of cardiac alternans was the discovery of subcellular  $\text{Ca}^{2+}$  alternans (Shiferaw and Karma, 2006; Rovetti et al., 2010; Qu et al., 2013; Gaeta et al., 2009; 2010; Gaeta and Christini, 2012; Restrepo and Karma, 2009; Aistrup et al., 2009). Originally, cardiac alternans were reported at the whole cell level where the  $\text{Ca}^{2+}$  concentration was averaged across the cell. With the advent of high-speed confocal microscopy, spatio-temporal structures of the intracellular  $\text{Ca}^{2+}$  concentration have been revealed where different parts of the cell exhibit out-of-phase alternations of the  $\text{Ca}^{2+}$  concentration. In a typical example, the right half of a ventricular myocyte displays large amplitude  $\text{Ca}^{2+}$  transients, while the amplitudes are small in the left half (Krogh-Madsen and Christini, 2012). On the next beat, this reverses, with small amplitude transients in the right half and large amplitudes in the left half. These alternans result from instabilities of single  $\text{Ca}^{2+}$  release units (CRUs), which comprise essential components of the  $\text{Ca}^{2+}$  signalling toolbox in the dyadic junction such as the L-type  $\text{Ca}^{2+}$  channel or the ryanodine receptor (RyR) (Krogh-Madsen and Christini, 2012; Qu et al., 2013). In healthy conditions, each CRU follows a regular period-1 orbit with the same amplitude of the  $\text{Ca}^{2+}$  transient at each heartbeat. It is this regularity that ensures high fidelity contraction of the cardiac

\* Corresponding author.

E-mail address: [ruediger.thul@nottingham.ac.uk](mailto:ruediger.thul@nottingham.ac.uk) (R. Thul).

muscle (Bers, 2002; 2008). Under pathological conditions, this period-1 orbit destabilises, giving rise to an orbit where  $\text{Ca}^{2+}$  amplitudes alternate in magnitude on successive heartbeats. These single node alternans then feed forward to the whole cell to produce macroscopic  $\text{Ca}^{2+}$  alternans exemplified by the left-right pattern mentioned above. Crucially, there is now compelling evidence that these subcellular  $\text{Ca}^{2+}$  alternans can induce travelling  $\text{Ca}^{2+}$  waves, which in turn can initiate arrhythmogenic afterdepolarisations (Kockskämper and Blatter, 2002; Diaz et al., 2002; Blatter et al., 2003).

An innovative analysis technique recently revealed a more granular view on subcellular  $\text{Ca}^{2+}$  alternans (Tian et al., 2012). For moderate pacing periods, whole cell  $\text{Ca}^{2+}$  transients appeared regular, suggesting a healthy ventricular myocyte. However, single CRU recordings identified alternating  $\text{Ca}^{2+}$  patterns, demonstrating that the cell was already pathological. To emphasise the fact that these  $\text{Ca}^{2+}$  alternans occur at single CRUs, they were termed microscopic  $\text{Ca}^{2+}$  alternans. To date, microscopic  $\text{Ca}^{2+}$  alternans constitute the earliest precursor for cardiac arrhythmias, which renders a comprehensive understanding of their emergence a crucial challenge in achieving cardiac well-being.

In the present work, we use a modelling framework to explore the onset of microscopic  $\text{Ca}^{2+}$  alternans in more detail. In particular, we are interested in how the coupling between individual CRUs drives this arrhythmia. We therefore focus on  $\text{Ca}^{2+}$  diffusion in the cytosol and the sarcoplasmic reticulum (SR) to better characterise this *network* effect. Commonly, subcellular  $\text{Ca}^{2+}$  alternans have been studied either through direct numerical simulations or by investigating low-dimensional maps (Gaeta et al., 2010; Shiferaw and Karma, 2006; Qu et al., 2013). Here, we use a different approach. We employ a piecewise linear (PWL) caricature (Thul and Coombes, 2010) of a well-established  $\text{Ca}^{2+}$  cycling model (Shiferaw et al., 2003). In turn, this allows us to perform a linear stability analysis of the *entire* network in a semi-analytical manner without the need to reduce the number of equations. Moreover, we can explicitly compute the eigenvector associated with the eigenvalue that leaves the unit disk – hence signalling the onset of an instability – which predicts the spatial patterns of the microscopic  $\text{Ca}^{2+}$  alternans very well.

The impact of  $\text{Ca}^{2+}$  diffusion on the formation of  $\text{Ca}^{2+}$  alternans has been studied before both at the level of a single CRU (where diffusion acts between different compartments of the CRU model) and entire CRU networks (Cantalapiedra et al., 2017; Restrepo et al., 2008). As with other changes that lead to  $\text{Ca}^{2+}$  alternans such as steeper load-release functions, impaired sarcoplasmic  $\text{Ca}^{2+}$  ATPase (SERCA) pumps or refractoriness of the RyR (Alvarez-Lacalle et al., 2013; Tomek et al., 2018; Huertas et al., 2010; Nivala and Qu, 2012; Rovetti et al., 2010; Qu et al., 2016; Díaz et al., 2004; Li et al., 2009),  $\text{Ca}^{2+}$  alternans usually emerge via a period-doubling bifurcation in this case. An exception can be found in (Cantalapiedra et al., 2017), where for a single CRU  $\text{Ca}^{2+}$  alternans emerge via a saddle-node bifurcation. Here, we report a novel route to microscopic  $\text{Ca}^{2+}$  alternans. For strong luminal coupling, we observe a saddle-node bifurcation at the *network level*, where an eigenvalue leaves the unit disk through (+1) along the real axis. In contrast to a period-doubling bifurcation (where an eigenvalue leaves at -1), which we also found in the case of strong cytosolic coupling, individual CRUs follow a period-1 orbit, but the amplitudes of neighbouring CRUs alternate. Hence, while the global cellular  $\text{Ca}^{2+}$  patterns are similar for  $\text{Ca}^{2+}$  alternans that emerge via a period-doubling and saddle-node bifurcation, respectively, the subcellular  $\text{Ca}^{2+}$  pattern is distinct. This shows that microscopic  $\text{Ca}^{2+}$  alternans exhibit rich dynamics, and consequentially the route to cardiac arrhythmias can proceed along more ways than previously established.

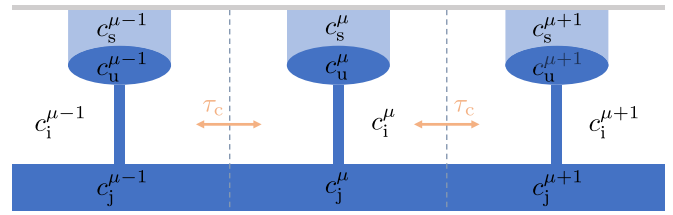


**Fig. 1. Schematic of a 1D CRU network.** Three CRUs with network label  $\mu - 1$ ,  $\mu$  and  $\mu + 1$  are shown. The grey line at the top corresponds to the sarcolemmal membrane, the light blue areas denote the subsarcolemmal space within the dyadic clefts, and the SR is coloured in blue. For the definition of the different  $\text{Ca}^{2+}$  concentrations, see Materials and Methods. The pale orange arrows denote diffusive coupling through the bulk cytosolic  $\text{Ca}^{2+}$  concentration with strength  $\tau_c$ . (For interpretation of the references to colour in this figure legend, the reader is referred to the web version of this article.)

## 2. Results

### 2.1. One dimensional CRU network

We first investigate a one-dimensional (1D) network consisting of 75 CRUs corresponding to 75 sarcomeres paced at  $T_p = 0.9$  s. Fig. 1 shows a schematic of three connected CRUs in such a network.

When  $\text{Ca}^{2+}$  diffusion in the cytosol is weak, the network exhibits synchronous  $\text{Ca}^{2+}$  release. Fig. 2A and B illustrate this by showing that the time evolution of the  $\text{Ca}^{2+}$  concentration in both the bulk cytosol and the SR for two neighbouring CRUs is identical. The bar plot in Fig. 2C summarises this for the 10 innermost CRUs of the network. When we increase the cytosolic diffusion strength, i.e. make  $\tau_c$  smaller, we observe the emergence of subcellular  $\text{Ca}^{2+}$  alternans as illustrated in Fig. 2D–F. It is worth noting that in the absence of diffusion, each CRU follows a stable period-1 orbit that is identical to the synchronous network state displayed in Fig. 2A and B. In other words, the emergence of the subcellular  $\text{Ca}^{2+}$  alternans is a pure network effect and not the result of changes in the local dynamics of the CRUs. Since we are interested in the onset of  $\text{Ca}^{2+}$  alternans, the difference in maxima between the small and large amplitude oscillations is small. However, if we move further beyond the instability, this difference becomes more pronounced and corresponds to observed changes of the intracellular  $\text{Ca}^{2+}$  concentration.

It is worth noting that the global  $\text{Ca}^{2+}$  concentration, i.e. the  $\text{Ca}^{2+}$  concentration averaged over the entire CRU network, remains unchanged irrespective of whether subcellular  $\text{Ca}^{2+}$  alternans exist or not (see Fig. S1). In other words, the global  $\text{Ca}^{2+}$  concentration does not predict if pathological  $\text{Ca}^{2+}$  alternans are present.

We can further quantify the onset of subcellular  $\text{Ca}^{2+}$  alternans by computing the eigenvalues of the linearised network equations. Fig. 3A shows the eigenvalues corresponding to the dynamics plotted in Fig. 2A–C. All eigenvalues are contained within the unit disk, indicating that the synchronous network state is linearly stable. As we increase the diffusive coupling, an eigenvalue passes through (-1) along the real axis, which signals the onset of  $\text{Ca}^{2+}$  alternans, see Fig. 3B and C. A further strengthening of the cytosolic diffusion leads to more eigenvalues leaving the unit disk as exemplified in Fig. 3D.

A strength of the PWL framework employed here is that we can compute the eigenvectors associated with the eigenvalues and compare them with the actual spatial  $\text{Ca}^{2+}$  concentration profile. In Fig. 4A we plot the peak subsarcolemmal  $\text{Ca}^{2+}$  concentration during one beat across the entire 75 CRU network when only one eigenvalue lies outside the unit disk. The alternations in the  $\text{Ca}^{2+}$  concentration are clearly visible. At the same time, the difference

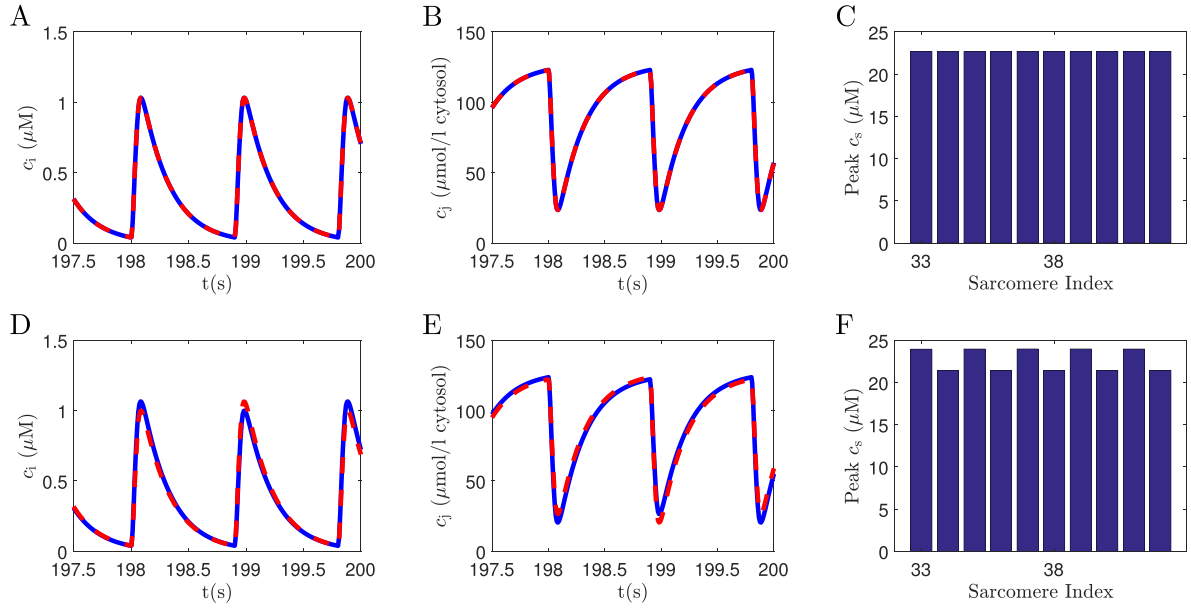


**Fig. 2. Emergence of alternans in a 1D network.** Bulk cytosolic  $\text{Ca}^{2+}$  concentration (A, D) and SR  $\text{Ca}^{2+}$  concentration (B, E) of two neighbouring CRUs (solid blue and dashed red, respectively) in a 1D network containing 75 CRUs at a pacing period of  $T_p = 0.9$  s and cytosolic coupling of strength  $\tau_c = 3$  s (top),  $\tau_c = 2.301$  s (bottom). Corresponding peak subsarcolemmal  $\text{Ca}^{2+}$  concentrations (C, F) during one pacing period of the 10 innermost CRUs of the network. All other parameter values as in Tables S1–S5. (For interpretation of the references to colour in this figure legend, the reader is referred to the web version of this article.)

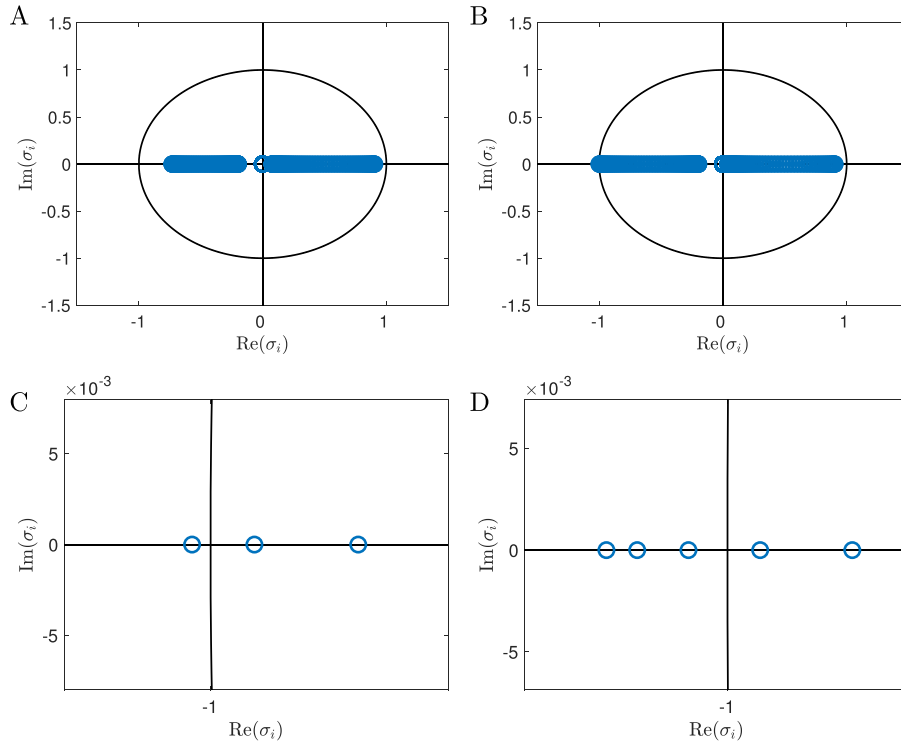


**Fig. 3. Eigenvalues in a 1D network.** (A)  $\tau_c = 3$  s, (B)  $\tau_c = 2.301$  s, (C) blow up of (B), (D)  $\tau_c = 2.29$  s. All other parameter values as in Tables S1–S5 and  $T_p = 0.9$  s.

in amplitude between neighbouring CRUs is maximal in the middle of the network and decreases towards the edges. This results from the no-flux boundary conditions of the network, which mimic the physical cell boundaries at either end of the cell. We observe no tapering of the amplitudes when we implement periodic boundary conditions (see Fig. S2). Fig. 4B displays the eigenvector that corresponds to the single eigenvalue that lies outside the unit disk in Fig. 3C. Its shape mirrors the pattern of the peak subsarcolemmal  $\text{Ca}^{2+}$  concentration shown in Fig. 4A, which demonstrates that

we can use the eigenvector to predict the  $\text{Ca}^{2+}$  concentration profile across the network after the onset of the instability. It is worth emphasising that this calculation is feasible because we can explicitly construct the matrix of the linearised network equations based on the semi-analytical solution for the synchronous network state (see Materials and Methods).

One of the reasons for predicting the shape of the subcellular  $\text{Ca}^{2+}$  alternans in Fig. 4 is that only one eigenvalue lies outside the unit disk. However, when we increase the diffusive

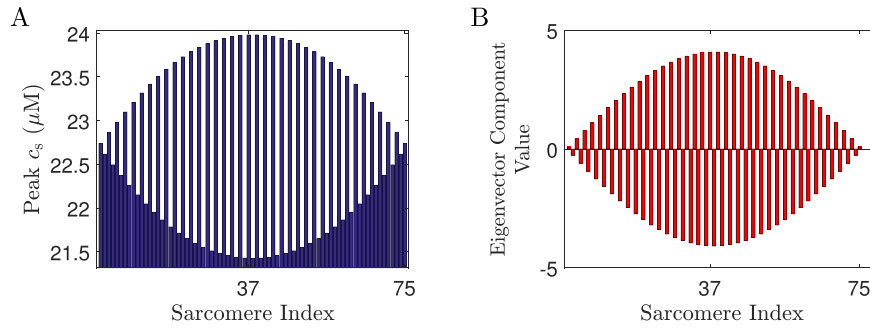


**Fig. 4. Eigenvector prediction close to alternans onset.** (A) Peak subarcolemmal  $\text{Ca}^{2+}$  concentration for  $\tau_c = 2.301$  s during one pacing period of the full 75 CRU network of Fig. 2D–F. (B) Eigenvector corresponding to the single eigenvalue that has left the unit disk in Fig. 3C. All other parameter values as in Tables S1–S5.

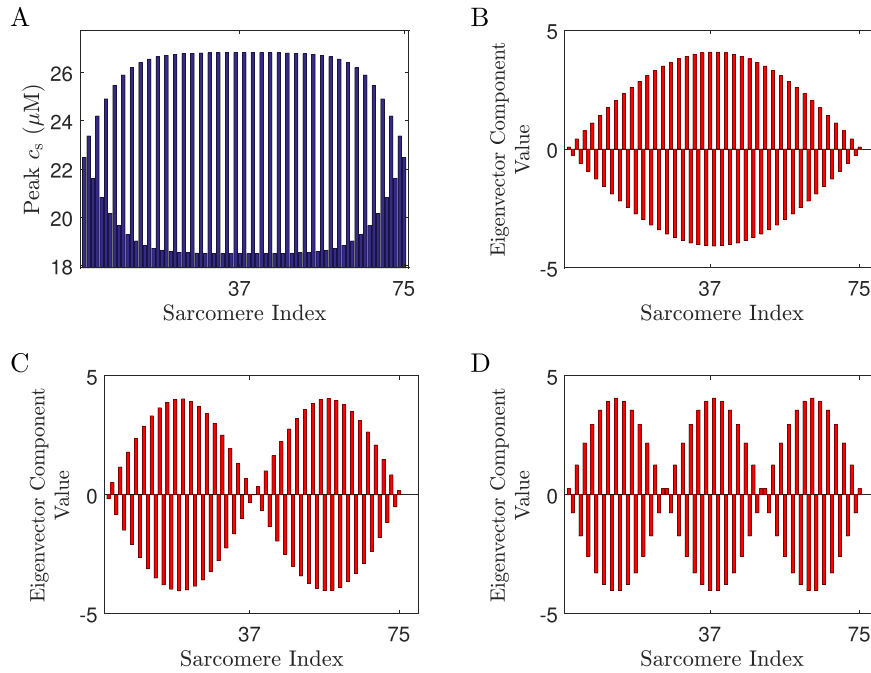


**Fig. 5. Critical eigenvectors further from alternans onset.** (A) Peak subarcolemmal  $\text{Ca}^{2+}$  concentration during one stimulus period for  $\tau_c = 2.29$  s. (B–D) Eigenvectors corresponding to the three eigenvalues outside the unit disk shown in Fig. 3D. All other parameter values as in Tables S1–S5.

coupling strength, more eigenvalues exit through the unit circle, see e.g. Fig. 3D. Would the eigenvectors for these three eigenvalues still predict the emergent  $\text{Ca}^{2+}$  pattern? Fig. 5 shows the corresponding  $\text{Ca}^{2+}$  concentration profile together with the three eigenvectors associated with the corresponding eigenvalues. At first sight, none of the individual eigenvectors recover the shape of the simulated  $\text{Ca}^{2+}$  concentration profile. Compared to Fig. 4A, the region where the amplitude between next-nearest neighbours stays constant is much extended, and the decrease in amplitude difference towards the edges of the network occurs over a much smaller number of CRUs. The tapering of the leading eigenvector shown in Fig. 5B is too strong to account for this behaviour, and the remaining two eigenvectors in Fig. 5C and D are multimodal, while the actual  $\text{Ca}^{2+}$  concentration profile is unimodal.

Because the eigenvectors are solutions to the linearised equations, superposition holds. We therefore tested whether a suitable combination of eigenvectors can reproduce the observed spatial pattern in Fig. 5A. As Fig. 6 reveals, adding the three eigenvectors with suitable weights to the synchronous network state approximates the actual  $\text{Ca}^{2+}$  concentration profile well. The superposition displays more undulations towards the centre of the network. This is understandable since the validity of the linear theory decreases the further we move away from the onset of the instability.

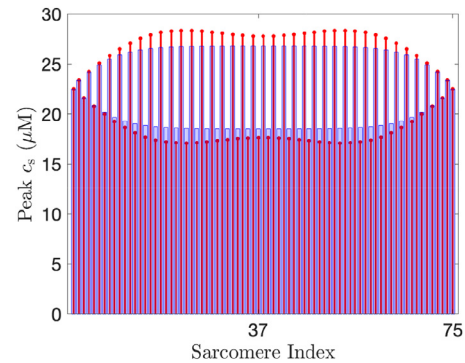


**Fig. 6. Eigenvector prediction further from alternans onset.** Bar plot (pale blue) of peak subarcolemmal  $\text{Ca}^{2+}$  concentration from a simulation in a network of 75 CRUs with  $T_p = 0.9$  s and  $\tau_c = 2.29$  s. The overlaid stencil plot (red) shows a linear combination of the eigenvectors added to the uncoupled peak subarcolemmal  $\text{Ca}^{2+}$  concentration for the same system. All other parameter values as in Tables S1–S5. (For interpretation of the references to colour in this figure legend, the reader is referred to the web version of this article.)

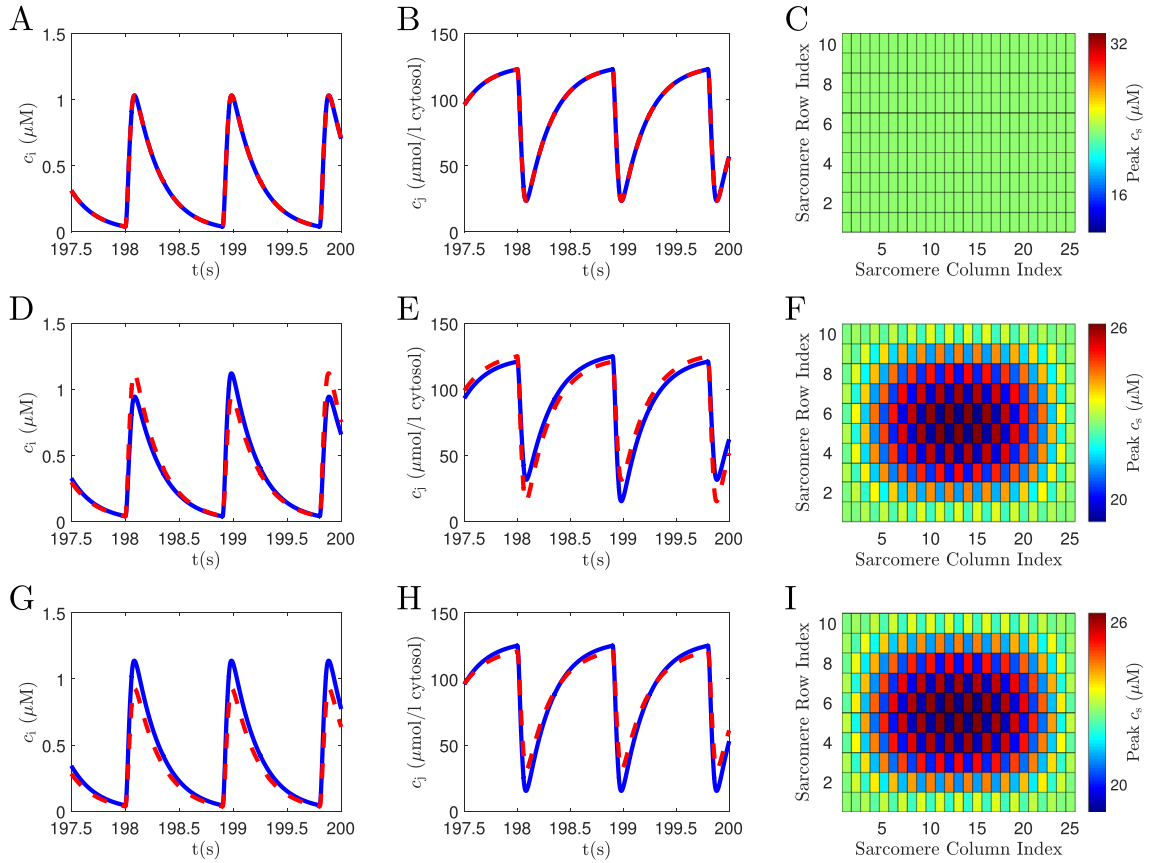


**Fig. 7. Emergence of alternans in a 2D network.** Bulk cytosolic  $\text{Ca}^{2+}$  concentration (A, D, G) and SR  $\text{Ca}^{2+}$  concentration (B, E, H) of two neighbouring CRUs (solid blue and dashed red, respectively) in a 2D network containing 250 CRUs for  $\tau_c = 5$  s,  $\tau_{sr} = 100$  s (top),  $\tau_c = 4.53$  s,  $\tau_{sr} = 100$  s (middle) and  $\tau_c = 100$  s,  $\tau_{sr} = 25.3$  s. Corresponding peak subsarcolemmal  $\text{Ca}^{2+}$  concentrations (C, F, I) during one pacing period for the entire network. All other parameter values as in Tables S1-S5 and  $T_p = 0.9$  s. (For interpretation of the references to colour in this figure legend, the reader is referred to the web version of this article.)

Taken together, the above findings demonstrate that our modelling approach captures the onset of subcellular  $\text{Ca}^{2+}$  alternans in the entire 75 CRU network, and that we can use the eigenvectors corresponding to the eigenvalues that have left the unit disk to predict the pattern of the subcellular  $\text{Ca}^{2+}$  alternans that emerges after the onset of the instability.

## 2.2. Two dimensional CRU networks

We next study two-dimensional (2D) networks containing 250 CRUs in a  $10 \times 25$  grid. In contrast to the results for the 1D case where we included only cytosolic coupling between neighbouring CRUs, we now allow for diffusive coupling through both the cytosol and the SR. As a control case, we first consider weak coupling in both compartments. Fig. 7A and B show the bulk cytosolic and the SR  $\text{Ca}^{2+}$  concentration for adjacent CRUs, respectively. Both CRUs behave identically, which suggests that the network has settled into stable synchrony. This is confirmed by plotting the peak subsarcolemmal  $\text{Ca}^{2+}$  concentration during one pacing period for the entire network, which does not exhibit any spatial structure. Starting from this control case, we first increase the strength of cytosolic coupling, i.e. we lower  $\tau_c$ .

As with the 1D case, the synchronous network state becomes unstable giving rise to subcellular  $\text{Ca}^{2+}$  alternans. Fig. 7D and E display the telltale alternations in the peak amplitudes in successive beats and show that neighbouring CRUs are out-of-phase with each other. The plot of the peak subsarcolemmal  $\text{Ca}^{2+}$  concentration during one beat across the entire network in Fig. 7F provides further evidence of this. We again note that the difference in am-

plitude between adjacent CRUs is most pronounced in the centre and decreases towards the edges. As for the 1D network, this results from the no-flux boundary conditions. When we increase the luminal coupling and keep the cytosolic coupling weak, we observe a novel form of subcellular  $\text{Ca}^{2+}$  alternans. Fig. 7G and H demonstrate that each CRU follows a stable period-1 orbit – the maxima of the blue trace remain constant across time, so do the amplitudes of the red dashed trace. However, the red dashed trace has a lower maximal value than the blue solid trace, indicating that the amplitude of the oscillations alternates between adjacent CRUs. Therefore, plotting the peak subsarcolemmal  $\text{Ca}^{2+}$  concentration during one pacing period yields the same plot as for dominant cytosolic coupling, i.e. the global  $\text{Ca}^{2+}$  pattern remains the same. What changes is the local dynamical behaviour.

To elucidate where this new behaviour originates from we plot the eigenvalues in both cases. Fig. 8A and B reveal that for dominant cytosolic coupling an eigenvalue crosses through  $(-1)$  along the real axis, giving rise to the standard period doubling bifurcation. In contrast, dominant luminal coupling results in an eigenvalue leaving the unit disk through  $(+1)$ . Therefore, the novel form of subcellular  $\text{Ca}^{2+}$  alternans is coordinated by a non-canonical bifurcation for cardiac arrhythmias, i.e. a saddle-node bifurcation. As Fig. 8B and E show, only one eigenvalue leaves the unit disk. Hence, we computed the associated eigenvectors, which are plotted in Fig. 8C and F, respectively. As in the 1D case, we find that the eigenvectors correctly predict the spatial patterns of the subcellular  $\text{Ca}^{2+}$  alternans, in particular the larger differences in amplitude towards the centre of the cell and the tapering off towards the edges. Note that the emergence of a saddle-node bifurcation at

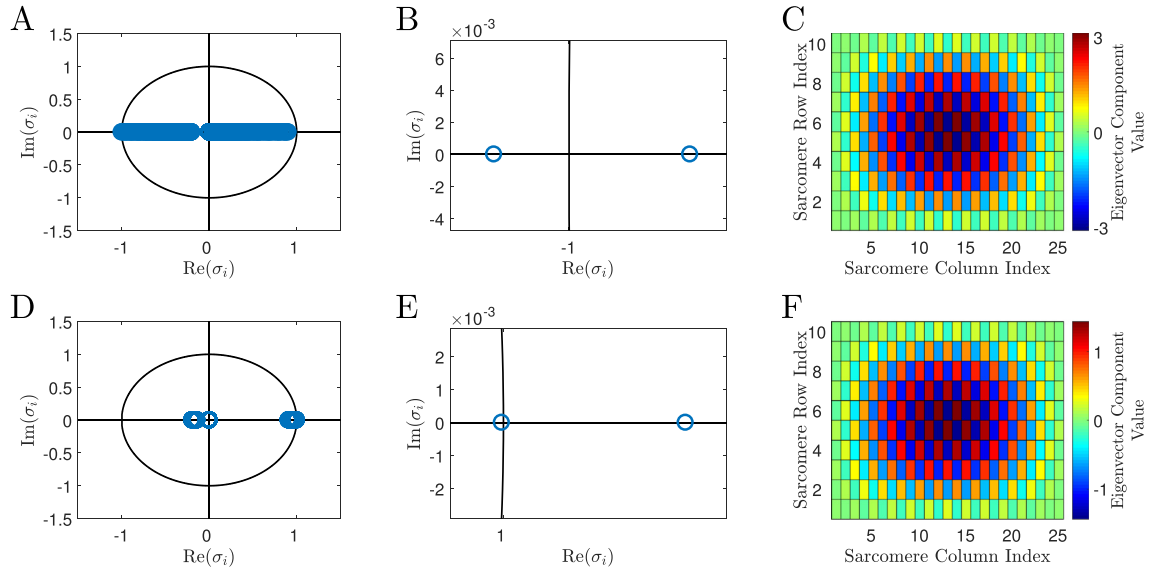


**Fig. 8. Eigenvalues and eigenvectors in a 2D network.** (A–C)  $\tau_c = 4.53$  s and  $\tau_{sr} = 100$  s and (D–F)  $\tau_c = 100$  s and  $\tau_{sr} = 25.3$  s, corresponding to Fig. 7D–F and Fig. 7G–I, respectively. The left column shows all eigenvalues, the middle column is a blow-up around  $-1$  (B) and  $+1$  (E), and the right column shows the eigenvector associated with the eigenvalue that left the unit disk.

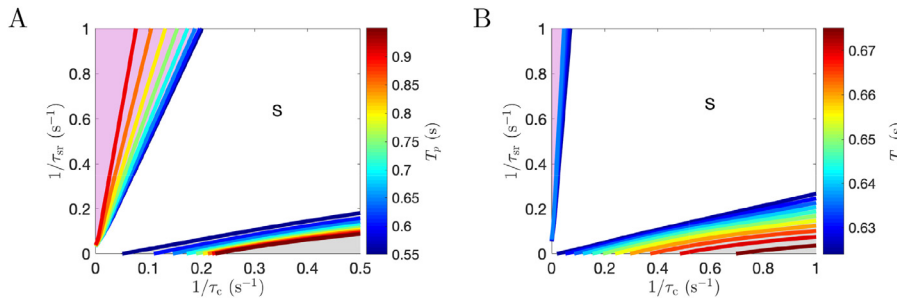


**Fig. 9. Bifurcation diagram** The lines delineate regions of stability, with different colours representing different pacing periods. Above and to the right, the synchronous state is stable (indicated by the letter S), while below and to the left,  $\text{Ca}^{2+}$  alternans exist. The lines stemming from the y axis (in the purple coloured region) refer to saddle-node bifurcations, those originating from the x axis (in the grey coloured region) to period doubling bifurcations. All parameter values as in Tables S1–S5 except (A)  $\nu_{up} = 405$  s $^{-1}$  and (B)  $\nu_{up} = 250$  s $^{-1}$ . (For interpretation of the references to colour in this figure legend, the reader is referred to the web version of this article.)

the network level is a consequence of the strong luminal coupling and not of the dimensionality of the network. As Fig. S3 illustrates, saddle-node bifurcations also occur in 1D networks with dominant SR coupling.

Given a set of parameter values, the computation of the eigenvalues for the linearised network dynamics is straightforward. However, we can also invert this approach and determine the parameter values that correspond to a certain bifurcation. Because of the PWL character of the model, this problem is computationally inexpensive, which allows us to construct bifurcation diagrams as plotted in Fig. 9. Here, we show the regions of stability and instability in the  $1/\tau_{sr}$  and  $1/\tau_c$  plane. We chose to use the reciprocal of the coupling strengths because when both of them vanish, the network is uncoupled. Hence, starting from  $(\tau_c^{-1}, \tau_{sr}^{-1}) = (0, 0)$  any increase along the axes corresponds to an increase in the coupling strength. Focussing first on Fig. 9A, we observe that when we keep  $1/\tau_c$  small and increase  $1/\tau_{sr}$ , we first hit one of the straight lines that stems from the y axis (in the purple coloured region).

These lines correspond to saddle-node bifurcations, and the different colours represent different pacing periods. We find that the longer the pacing period, the stronger luminal diffusion has to be for the onset of  $\text{Ca}^{2+}$  alternans. This follows directly from the fact that the slope of the straight line is larger for longer pacing periods compared to that for shorter periods; see e.g. the blue curve

for  $T_p = 0.6$  s and the red curve for  $T_p = 0.9$  s. On the other hand, when  $1/\tau_{sr}$  is small and  $1/\tau_c$  is increased, we encounter the lines that originate from the x axis (in the grey coloured region). These are period-doubling bifurcations, and as for the saddle-node bifurcation,  $\text{Ca}^{2+}$  alternans only emerge for stronger coupling when the pacing period gets longer. This behaviour differs from when  $1/\tau_{sr}$  takes on intermediate or larger values in the diagram, e.g.  $1/\tau_{sr} = 0.5$  s $^{-1}$ . Here, for vanishing cytosolic coupling, the synchronous network state is unstable and only gains stability for larger values of cytosolic diffusion. The same holds true for larger values of  $1/\tau_c$  and an increase of  $1/\tau_{sr}$ . First, synchrony is unstable and only stabilises above the period-doubling bifurcation line. In general, we see that when the coupling is balanced, i.e.  $1/\tau_c$  and  $1/\tau_{sr}$  are of similar magnitude, the synchronous network state is stable. For Fig. 9B, we repeat the calculation, but with weaker SERCA pumps. We again observe straight lines originating from the axes, with lines indicating saddle-node bifurcations starting from the y axis (purple coloured region) and those signalling a period-doubling bifurcation stemming from the x axis (grey coloured region). Also, longer pacing periods can tolerate stronger coupling strengths before the onset of  $\text{Ca}^{2+}$  alternans. The main difference between Fig. 9A and B is the range of the pacing periods. While in the former, we cover more than 0.3 s, in the latter, there is little variation.

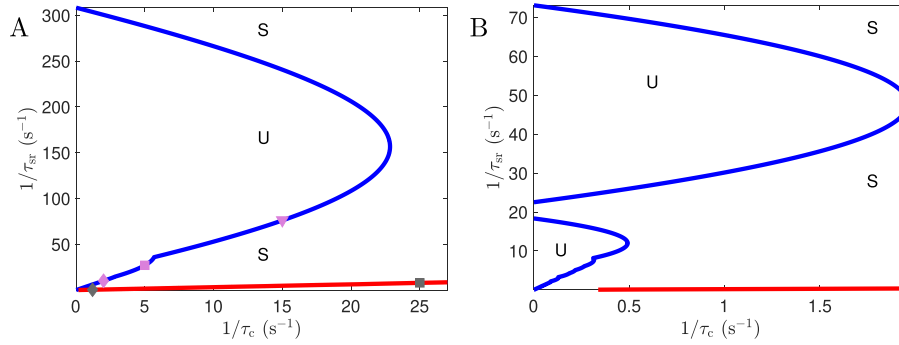


**Fig. 10. Bifurcation diagram** Plots showing the values of  $\tau_{sr}^{-1}$  and  $\tau_c^{-1}$  at which the synchronised network state undergoes a bifurcation at fixed pacing periods of  $T_p = 0.6$  s (A) and  $T_p = 0.95$  s (B) in a network of 250 CRUs. In regions labelled S the synchronised network state is stable, whilst it is unstable in regions labelled U. The blue line marks the values for a saddle-node bifurcation and the red line is for a period-doubling bifurcation. The symbols in panel (A) refer to the parameter values used in Figs. 11 and 12. All other parameter values as in Tables S1–S5. (For interpretation of the references to colour in this figure legend, the reader is referred to the web version of this article.)

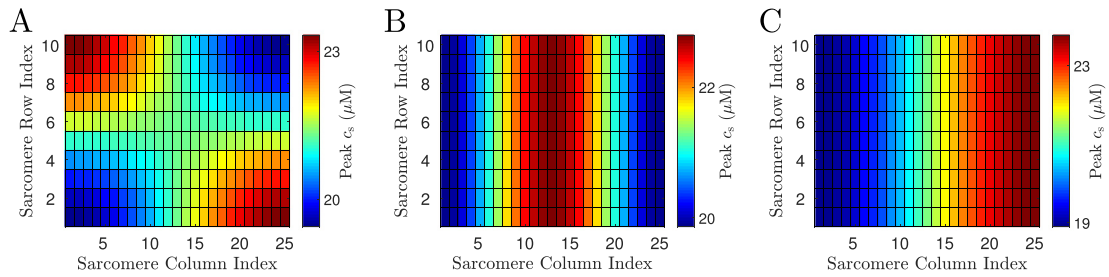


**Fig. 11. Subcellular  $Ca^{2+}$  alternans for dominant SR coupling** Plots showing the peak subsarcolemmal  $Ca^{2+}$  concentrations from a single pacing period in a network of 250 CRUs with pacing period  $T_p = 0.6$  s. The coupling parameters are  $\tau_{sr}^{-1} = 203/20$   $s^{-1}$  and  $\tau_c^{-1} = 2$   $s^{-1}$  (A),  $\tau_{sr}^{-1} = 676/25$   $s^{-1}$  and  $\tau_c^{-1} = 5$   $s^{-1}$  (B),  $\tau_{sr}^{-1} = 76.33$   $s^{-1}$  and  $\tau_c^{-1} = 15$   $s^{-1}$  (C). These values correspond to the purple diamond, square and triangle in Fig. 10A, respectively. All other parameter values as in Tables S1–S5. (For interpretation of the references to colour in this figure legend, the reader is referred to the web version of this article.)

In Fig. 9, we focus on the region around the origin in the  $1/\tau_c$  and  $1/\tau_{sr}$  plane to elucidate the behaviour for the onset of coupling. In Fig. 10, we take a wider look as can be deduced from the increased axis ranges. Fig. 10A shows the saddle-node bifurcation line in blue and the period-doubling bifurcation line in red for a fixed pacing period of  $T_p = 0.6$  s. When we fix a cytosolic diffusion strength and increase luminal coupling, the synchronous network is stable above the red period doubling bifurcation line and unstable below it, in accordance with the results shown in Fig. 9. For smaller values of  $1/\tau_c$ , we enter a region of instability via a saddle-node bifurcation, before leaving it again via a saddle-node bifurcation into a region of stability. In contrast, when luminal coupling is constant and we make cytosolic diffusion stronger, the synchronous network state is first unstable before gaining stability through a saddle-node bifurcation. Upon increasing the pacing period, the bifurcation diagram develops additional structures as illustrated in Fig. 10B. For larger values of cytosolic coupling, we again find regions where when increasing luminal coupling, the synchronous network state is first stable, then unstable and finally stable again. But for weaker coupling in the cytosol, an additional region of unstable solutions bounded by a saddle-node bifurcation emerges.

It is now instructive to explore the patterns of the  $Ca^{2+}$  concentration in the vicinity of the bifurcation lines. In Fig. 11, we plot three examples of the peak subsarcolemmal  $Ca^{2+}$  concentration at one beat as we move along the lower part of the blue saddle-node bifurcation line in Fig. 10A. All three cases depict subcellular  $Ca^{2+}$  alternans, but the patterning is distinct. For the weakest coupling shown in Fig. 11A, adjacent corners of the cell oscillate with different amplitudes, while the dynamics of the  $Ca^{2+}$  concentration in opposing corners is identical. In the intermediate case in Fig. 11B, the peak values in the centre of the cell are larger than those at

the periphery, while for stronger coupling, the cell exhibits a left-right asymmetry. Note that the stripes in the last two cases run parallel to the short axis of the cell, i.e. the variation occurs along the long cell axis.

Given that the patterns of the subcellular  $Ca^{2+}$  alternans change as we traverse the saddle-node bifurcation line, we checked whether a similar behaviour occurs for the period-doubling bifurcation. Fig. 12 demonstrates that is indeed the case. Here, we plot the peak subsarcolemmal  $Ca^{2+}$  concentration at two subsequent beats as we move along the red line in Fig. 10A. For weaker cytosolic coupling, Fig. 12A and B illustrate complex microscale variations, with all CRUs oscillating out-of-phase with respect to their neighbours. As expected for a period doubling bifurcation, the  $Ca^{2+}$  concentration for a given CRU changes peak amplitude from one beat to the next, even for the green bands, where the difference in amplitude is small. Increasing the coupling changes the patterns completely. As Fig. 12D and E highlight, the wavelength of the pattern increases, with extended regions showing similar peak amplitudes. The pattern is reminiscent of the one observed in Fig. 11A. However, here, the corners at the top and at the bottom behave identically and are out-of-phase with respect to each other. Moreover, there are additional maxima and minima towards the centre of the cell. Since both patterns are characterised by a single eigenvalue that has left the unit disk, we plot the corresponding eigenvectors in Fig. 12C and F, respectively. Again, we observe excellent agreement between the eigenvector and the emerging pattern of the subcellular  $Ca^{2+}$  alternans.

All results so far have been obtained with the PWL model. The main reason for this is that we can explicitly perform the linear stability analysis, which has allowed us to unravel complex patterns of subcellular  $Ca^{2+}$  alternans. At this point, it stands to reason what impact the PWL caricature has on our findings. We

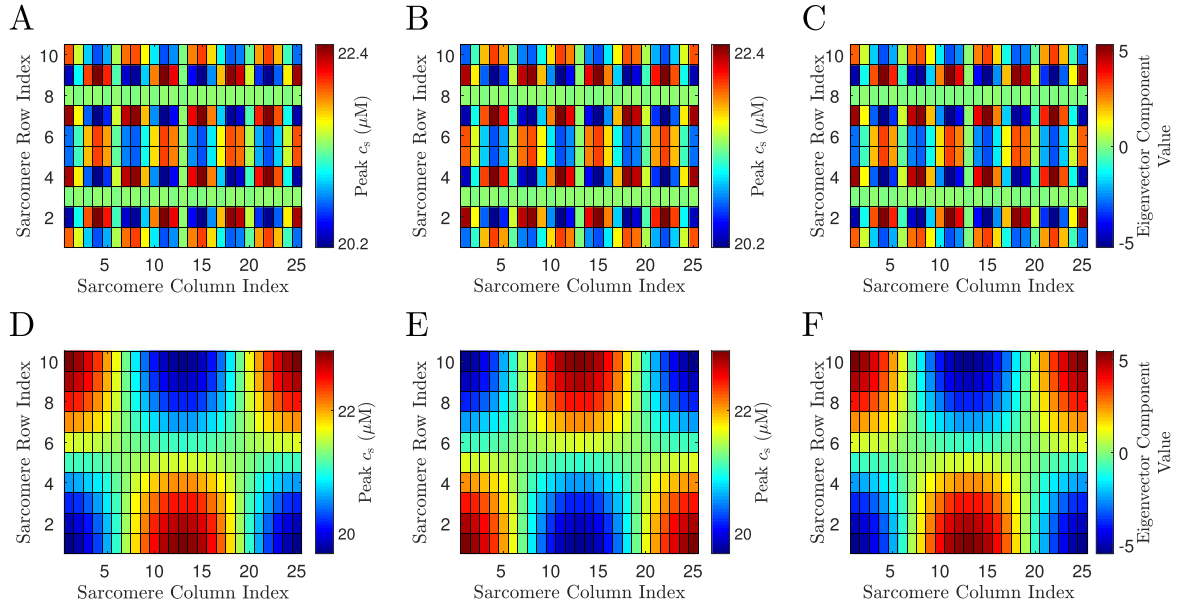


**Fig. 12. Subcellular  $\text{Ca}^{2+}$  alternans for dominant cytosolic coupling** Plots of the peak subarcolemmal  $\text{Ca}^{2+}$  concentration from two simulations of a 250 CRU network across two successive pacing periods. (A, D) represent the first pacing periods whilst (B, E) represent the second pacing period. For both these simulations  $T_p = 0.6$  s. In the top row,  $\tau_c^{-1} = 1.2$  s $^{-1}$  and  $\tau_{sr}^{-1} = 0.37745$  s $^{-1}$ , while in the bottom row  $\tau_c^{-1} = 25$  s $^{-1}$  and  $\tau_{sr}^{-1} = 393/50$  s $^{-1}$ . (C, F) show the eigenvector associated with the single eigenvalue that has left the unit disk corresponding to the simulations in (A,B) and (D, E), respectively. The coupling parameters for the top (bottom) are shown as grey diamond (square) in Fig. 10A. All other parameter values as in Tables S1–S5.

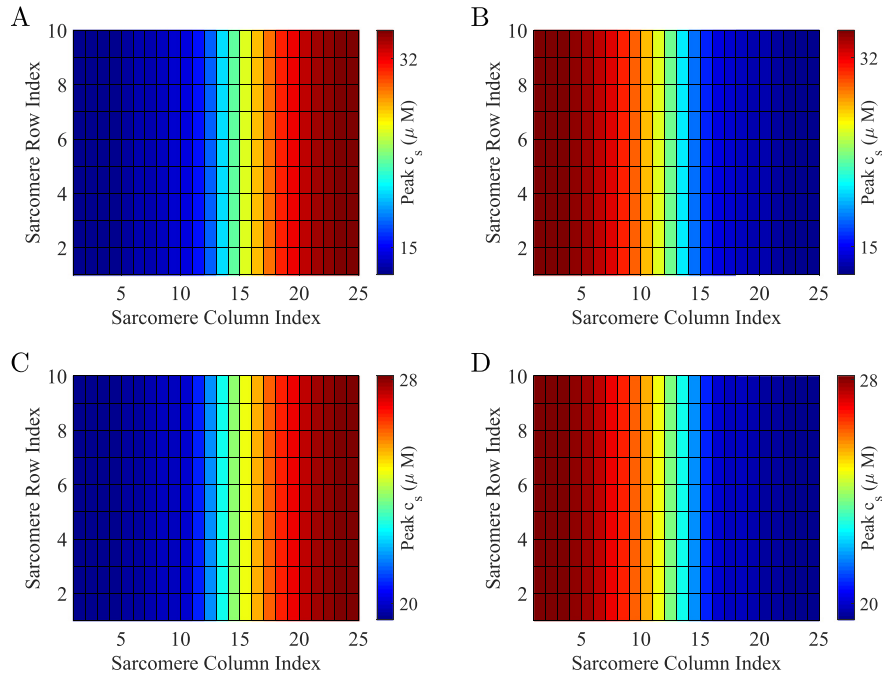


**Fig. 13. Comparison between PWL and nonlinear model** Plots of the peak subarcolemmal  $\text{Ca}^{2+}$  concentration for two consecutive pacing periods in a network of 250 CRUs for  $T_p = 0.6$  s. (A,B) show results for the PWL model, while (C,D) show results for the nonlinear model in Shiferaw et al. (2003) with clamped buffers. In both cases, the coupling is  $\tau_c = 37$  s $^{-1}$  and  $\tau_{sr} = 280$  s $^{-1}$ . In (C,D) we used  $\gamma = 4$  and  $i_{ca} = 6600 \mu\text{mol C}^{-1} \text{cm}^{-1}$ . All other parameter values as in Tables S1–S5.

therefore simulated the original model from Shiferaw et al. (2003) and compared it to our PWL model. Representative results are shown in Fig. 13. The patterns are almost identical, with the peak amplitudes in the PWL model slightly higher than in the original model.

The analysis technique that we have employed to determine linear stability in this study is general in that it can cope with any synchronous network state. The results above all pertain

to a synchronous network state with period 1. However, the model also supports a synchronous period-2 orbit as illustrated in Fig. 14, which corresponds to spatially concordant alternans (SCAs). Fig. 14A shows that the time course of the subarcolemmal  $\text{Ca}^{2+}$  concentration for two adjacent CRUs is identical, and when we plot the peak subarcolemmal  $\text{Ca}^{2+}$  concentration at two successive pacing periods we observe no spatial variation, but clear changes in the amplitude. Moreover, all eigenvalues are contained within

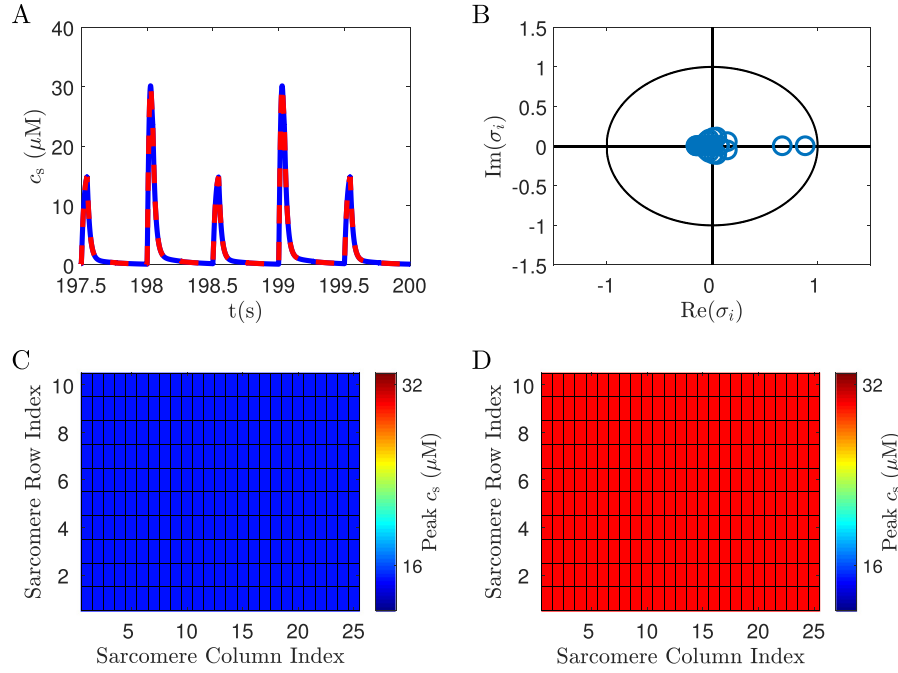


**Fig. 14. Stable spatially concordant alternans** (A) Trajectories from two neighbouring CRUs (solid blue and dashed red line, respectively) of the subarcolemmal  $Ca^{2+}$  concentration. (B) Plot of the eigenvalues of the system. (C, D) Plots of the peak subarcolemmal  $Ca^{2+}$  concentration across two successive pacing periods. The network contains 250 CRUs with coupling strengths  $\tau_c = 0.08$  s,  $\tau_{sr} = 0.2$  s and is simulated with pacing period  $T_p = 0.5$  s. All other parameter values as in Tables S1–S5. (For interpretation of the references to colour in this figure legend, the reader is referred to the web version of this article.)

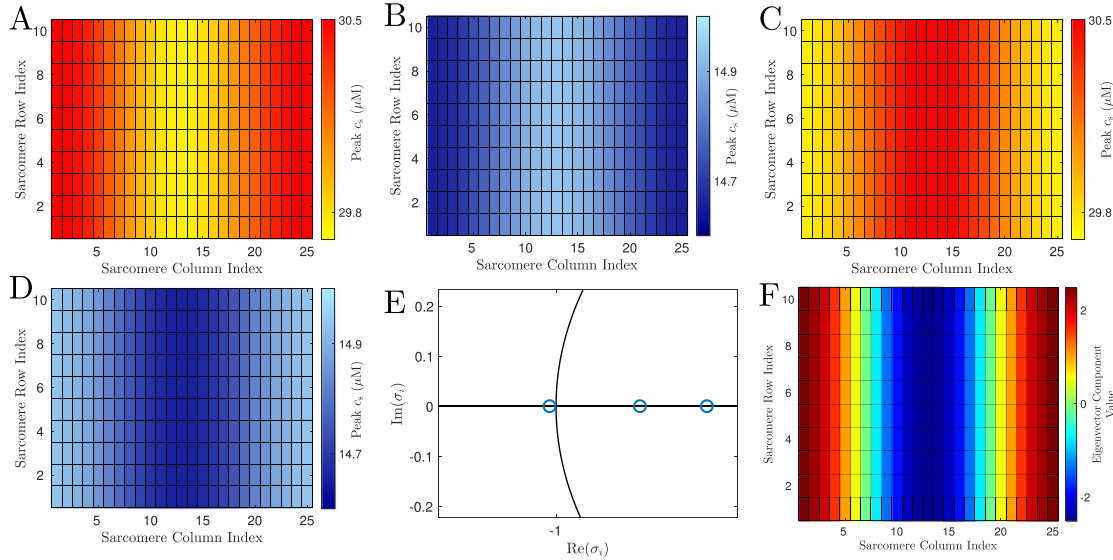


**Fig. 15. Instability of spatially concordant alternans** Peak subarcolemmal  $Ca^{2+}$  concentration from 4 consecutive pacing periods (A–D) of a network containing 250 CRUs with coupling strengths  $\tau_c = 0.012$  s,  $\tau_{sr} = 1.3$  s and simulated at a pacing period  $T_p = 0.5$  s. Also plotted are the key eigenvalues (E) and the eigenvector corresponding to the eigenvalue outside the unit disk (F). All other parameter values as in Tables S1–S5.

the unit disk as depicted in Fig. 14B, confirming that the pattern that we see is stable. We are now in the position to study the linear stability of these SCAs. When we increase the coupling strength in the cytosol, but decrease luminal coupling, we obtain a period-4 orbit as shown in Fig. 15. In Fig. 15A, we see that the peak amplitude of the subarcolemmal  $Ca^{2+}$  concentration during one pacing period develops a spatial pattern with stripes of larger amplitudes at the left and right edge of the cell and a lower peak amplitude in the centre. During the next pacing period (Fig. 15B) the stripes remain, but the peak amplitude is now larger in the centre com-

pared to the edges, and the values of the  $Ca^{2+}$  concentrations have almost halved. At the third pacing period, the range of the  $Ca^{2+}$  concentration corresponds to the one in the first pacing period, but now the peak amplitude is large in the centre and small at the periphery. Hence Fig. 15A and C as a pair would correspond to a period-2 orbit, but now they are two pacing periods apart. Finally, Fig. 15D shows a flipped case of Fig. 15B, concluding the sequence of the period-4 orbit. As Fig. 15E demonstrates, SCAs, i.e. the synchronous period-2 orbit, have indeed gone unstable via an eigenvalue crossing through  $-1$  along the real axis. Since only one

eigenvalue lies outside the unit disk, we compute the eigenvector associated with this eigenvalue. It is depicted in Fig. 15F and corresponds to the spatial pattern shown in Fig. 15A–D.

### 3. Discussion

Cardiac alternans present a severe disruption of the healthy cardiac rhythm. In particular, they often form precursors to fatal cardiac arrhythmias such as sudden cardiac death, which renders their understanding highly relevant for our well-being.

In this present study, we investigated the role of  $\text{Ca}^{2+}$  diffusion in both the cytosol and the SR in the formation of microscopic  $\text{Ca}^{2+}$  alternans (Tian et al., 2012), which form one of the earliest harbingers of cardiac arrhythmia. When cytosolic diffusion dominates,  $\text{Ca}^{2+}$  alternans are induced via the standard period-doubling bifurcation, where the critical eigenvalue passes through  $(-1)$  along the real axis (Figs. 3B and C, 8 A and B). For strong luminal diffusion, we uncovered a novel route to microscopic  $\text{Ca}^{2+}$  alternans via a saddle-node bifurcation, where an eigenvalue leaves the unit disk at  $(+1)$  (Fig. 8D and E). Globally, the emergent cell wide patterns of the  $\text{Ca}^{2+}$  concentration look similar (Fig. 8C and F), in that adjacent CRUs display alternating maxima of the  $\text{Ca}^{2+}$  concentration. The main difference lies in the temporal evolution of the  $\text{Ca}^{2+}$  concentration at individual CRUs. In the period-doubling case, each CRU exhibits alternating  $\text{Ca}^{2+}$  dynamics (Figs. 2D–F, 7 D and E) i.e. a period-2 orbit, while for the saddle-node bifurcation, each CRU follows a period-1 orbit, but the  $\text{Ca}^{2+}$  concentration at adjacent CRUs takes on different maximal values (Fig. 7G and H).

The microscopic  $\text{Ca}^{2+}$  alternans that have been measured so far (see e.g. Tian et al. (2012)) resemble the ones shown in Fig. 7D–F, where neighbouring sites exhibit alternating period-2 orbits that oscillate out-of-phase with respect to one another. Our theoretical results suggest that biological microscopic  $\text{Ca}^{2+}$  alternans may possess more complex patterns than previously thought. The hallmark of microscopic  $\text{Ca}^{2+}$  alternans is that whole cell  $\text{Ca}^{2+}$  signals look regular, while  $\text{Ca}^{2+}$  transients at individual CRUs already display pathological behaviour. For both the period-doubling and the saddle-node bifurcation, global signals would almost be indistinguishable. However, the local dynamical behaviour differs substantially as described above. This suggests that to more faithfully predict the onset of  $\text{Ca}^{2+}$  alternans, it is crucial to investigate a larger fraction of the CRU network. This will generate sufficient data to obtain high quality statistics on the peak amplitudes of  $\text{Ca}^{2+}$  transients, which is important since establishing a period-1 orbit for individual CRUs does not suffice to conclude healthy behaviour in light of the saddle-node bifurcation reported here.

Focussing on  $\text{Ca}^{2+}$  diffusion also addresses a still unanswered question in cardiac physiology: is  $\text{Ca}^{2+}$  diffusion in the SR slow or fast? Studies to date provide contradicting results (Swietach et al., 2008; Picht et al., 2011; Bers and Shannon, 2013). The findings reported here provide a possible avenue for distinguishing between these two hypotheses as different SR  $\text{Ca}^{2+}$  diffusion strengths lead to different microscopic  $\text{Ca}^{2+}$  alternans. For fast diffusion, we would expect microscopic  $\text{Ca}^{2+}$  alternans where CRUs follow a period-1 orbit, but with different peak amplitudes, while for slow SR diffusion, we should observe the well-known alternating  $\text{Ca}^{2+}$  concentration profiles at individual CRUs.

When investigating cardiac alternans, one is always confronted with the bidirectional coupling between membrane voltage and intracellular  $\text{Ca}^{2+}$ . Essentially, voltage dependent  $\text{Ca}^{2+}$  fluxes such as  $\text{Ca}^{2+}$  entry through the L-type  $\text{Ca}^{2+}$  channel or  $\text{Ca}^{2+}$  extrusion via the sodium-calcium exchanger (NCX) alter the intracellular  $\text{Ca}^{2+}$  concentration. In turn, the intracellular  $\text{Ca}^{2+}$  concentration feeds back to these AP-dependent pathways through e.g.  $\text{Ca}^{2+}$  dependent gating of the L-type  $\text{Ca}^{2+}$  channel and the NCX. To make progress,

both experimentally and theoretically, the AP is often clamped. We here followed this approach and considered a model of  $\text{Ca}^{2+}$  cycling only (Shiferaw et al., 2003; Thul and Coombes, 2010). In light of the discussion in Jordan and Christini (2007) our results therefore apply to the case when cardiac alternans are  $\text{Ca}^{2+}$ -driven.

The  $\text{Ca}^{2+}$  subsystem offers multiple ways of inducing  $\text{Ca}^{2+}$  alternans, including the activity levels of SERCA pumps, the load-release function of the SR and the refractoriness of the RyR (Alvarez-Lacalle et al., 2013; Tomek et al., 2018; Huertas et al., 2010; Nivala and Qu, 2012; Rovetti et al., 2010; Qu et al., 2016; Diaz et al., 2004; Li et al., 2009). These factors control the local behaviour of CRUs. We are interested in the network effects that contribute to the formation of subcellular  $\text{Ca}^{2+}$  alternans. Therefore, we focussed on the role of  $\text{Ca}^{2+}$  diffusion in both the cytosol and the SR, as it is  $\text{Ca}^{2+}$  diffusion that couples adjacent CRUs to form a network. For this endeavour to be meaningful, we assumed that a single uncoupled CRU follows a physiologically regular period-1 orbit and does not exhibit  $\text{Ca}^{2+}$  alternans. Indeed, most models for isolated CRUs can be driven into  $\text{Ca}^{2+}$  alternans by decreasing SERCA pump activity or steepening the load-release function for fixed pacing periods. However, if the local  $\text{Ca}^{2+}$  dynamics at a CRU is already unstable, observing  $\text{Ca}^{2+}$  alternans at the network level is less surprising. Consequentially, our findings are particularly relevant to any alterations that increase the propensity for inducing  $\text{Ca}^{2+}$  alternans at a single CRU as microscopic  $\text{Ca}^{2+}$  alternans are more likely in this case. Another reason for homing in on  $\text{Ca}^{2+}$  diffusion is that it is affected by endogenous and exogenous buffers such as dyes. Therefore, even if the local CRU dynamics would lead to healthy behaviour, buffers might change that.

A number of studies have investigated the formation of subcellular  $\text{Ca}^{2+}$  alternans. Conceptually, they fall into two main classes: either large-scale numerical simulations of CRU networks or reduced one- or two-dimensional maps. Here, we advocate a modelling philosophy that sits in the middle of these extremes. On the one hand, we would like to investigate the entire network without reducing the number of differential equations, hence incorporating the more realistic setup of large-scale simulations. On the other hand, we would like to exploit the mathematical tractability of low dimensional maps. We have achieved both aims by considering a PWL model of a CRU that we developed in Thul and Coombes (2010) and which is based on the established model of  $\text{Ca}^{2+}$  cycling in Shiferaw et al. (2003). This allows us to explicitly construct both period-1 and period-2 orbits for a single CRU, i.e. the healthy regular and the  $\text{Ca}^{2+}$  alternating rhythm, respectively. In turn, this provides the input for the stability approach developed in Pecora and Carroll (1998). As shown in Materials and Methods, we can explicitly construct the matrix  $S_m$  that relates some initial network perturbation  $\delta y_0$  to its final value  $\delta y_{m+1}$  after one pacing period, i.e.  $\delta y_{m+1} = S_m \delta y_0$ . The ability to compute  $S_m$  endows our modelling framework with the mathematical tractability typically associated with maps, while the entries of  $S_m$  encapsulate the dynamics of the entire network.

At this point, one might ask how well PWL models capture the dynamics of the associated nonlinear models. There is now a large body of evidence that shows that PWL models reproduce key features of their nonlinear counterparts. Of particular note is the McKean model (McKean, 1970), which constitutes a PWL caricature of the seminal Fitzhugh-Nagumo equations (FitzHugh, 1961; Nagumo et al., 1962) for neural activity. For the PWL model employed here, we demonstrated in Thul and Coombes (2010) that it reproduces both the physiological period-1 and the pathological alternating orbit of a single CRU. Moreover, Fig. 13 demonstrates that even at the network level the PWL model behaves almost identically to the original model. What does differ between the two modelling approaches are parameter values, which cannot necessarily be translated one-to-one from one model to the other. In this respect, PWL

models should be understood as a tool to probe the dynamical repertoire and explain in fundamental terms the behaviour of the full nonlinear system.

A defining characteristic of microscopic  $\text{Ca}^{2+}$  alternans is that they describe cardiac dynamics just after the point when the regular period-1 orbit of a CRU goes unstable (Tian et al., 2012). Our PWL model is ideally suited to zoom in on this. Firstly, we can trace the eigenvalues of the full network stability calculation to determine the exact moment when the network undergoes an instability. Secondly, we can compute the eigenvector that is associated with the eigenvalue that induces the instability. As Figs. 4B, 8 C and F, 12 C and F demonstrate, these eigenvectors provide a very good prediction of the emergent subcellular  $\text{Ca}^{2+}$  pattern. As soon as more than one eigenvector lies outside the unit disk, the emergent network pattern is a linear combination of the eigenvectors associated with these eigenvalues, see Figs. 5 and 6. In this case, the predictive power of the eigenvectors is limited as *a priori* we do not know their weights with which they enter the superposition. What these eigenvectors allow us, though, is to scan the patterns that could potentially emerge by exploring different linear combinations of these eigenvectors.

Since determining the eigenvalues and eigenvectors is numerically inexpensive, we computed bifurcation diagrams as plotted in Fig. 10. They show that the period doubling bifurcation and the saddle-node bifurcation both divide the parameter plane but that the former occurs under dominant cytosolic coupling and the latter when luminal diffusion is strong. Interestingly, the topology of the bifurcation diagrams changes as we alter the pacing period. In particular, we find additional lobes of unstable solutions as we increase the pacing period. Because of the predictive power of the eigenvectors close to the stability boundaries, we computed a series of them associated with the single eigenvalue that leaves the unit disk. We found that the patterns of the eigenvectors change significantly as we move along the stability boundaries. For instance, in the vicinity of the lower branch of saddle-node bifurcations in Fig. 10A, we find some checkerboard pattern of  $\text{Ca}^{2+}$  activity for weaker coupling strength (Figs. 11A), which changes into a pattern of stripes for stronger coupling (Figs. 11B) and then into a left-right asymmetry for even stronger coupling (Figs. 11C). What is remarkable is that there is no obvious ordering of these patterns, in that knowing one does not predict the next one as we increase the coupling. The point at which these patterns change sometimes coincides with a kink in the bifurcation line. For instance, we found such a change at the small cusp around  $1/\tau_c = 5$  on the lower saddle-node bifurcation line in Fig. 10A.

Some of the  $\text{Ca}^{2+}$  alternans that we have investigated can be classified as spatially discordant since different parts of the cell exhibit out-of-phase patterns with respect to their peak amplitudes (Weiss et al., 2006). For example, Figs. 11 and 12 demonstrate that during one pacing period, parts of the cell exhibit small amplitudes, while the amplitude is large in other parts. However, SCAs exist as well, where the peak amplitude is either small or large across the entire cell (Fig. 14). From a mathematical perspective, SCAs correspond to a synchronous network state. The only difference being that it is a period-2 orbit instead of a period-1 orbit. Importantly, our analysis works for any synchronous state. We therefore tested the linear stability of SCAs and found that they lose stability to a period-4 orbit (Fig. 15). Again, the eigenvector that is associated with the single eigenvalue that leaves the unit disk predicts the spatial pattern of the emergent period-4 orbit.

#### 4. Conclusion

We analysed the impact of cytosolic and luminal  $\text{Ca}^{2+}$  diffusion on the formation of subcellular  $\text{Ca}^{2+}$  alternans in 1D and 2D net-

works of CRUs. When cytosolic diffusion dominates,  $\text{Ca}^{2+}$  alternans emerge via a period-doubling bifurcation. Stronger diffusion in the SR leads to an instability via a saddle-node bifurcation, which to date has not been reported for  $\text{Ca}^{2+}$  alternans and which generates microscopic  $\text{Ca}^{2+}$  alternans that are distinct from the ones driven by a period-doubling bifurcation. The PWL modelling framework that we adopted allowed us to perform a linear stability analysis for the entire network *without* the reduction in the number of dynamical variables. As part of this, we computed the eigenvectors that are associated with the eigenvalues that leaves the unit disk and showed that they correctly predict the spatial patterns of the emergent subcellular  $\text{Ca}^{2+}$  alternans. Importantly, we found that these patterns vary substantially along bifurcation lines.

The pathways of the  $\text{Ca}^{2+}$  cycling model that we employ capture the core  $\text{Ca}^{2+}$  dynamics at a CRU. In a next step, it would be interesting to explore the impact of further  $\text{Ca}^{2+}$  dependent pathways on the generation of microscopic  $\text{Ca}^{2+}$  alternans, in particular the role of the refractory period of the RyR and of additional accessory proteins in the junctional SR such as triadin and junctin. In addition, our model is deterministic, but fluctuations based on the stochastic recruitment of RyRs is of central interest in the study of  $\text{Ca}^{2+}$  alternans. It will therefore be exciting to marry the random dynamics of RyRs with the PWL model employed here to unravel further the complex dynamics of subcellular  $\text{Ca}^{2+}$  alternans.

#### 5. Materials and Methods

We used the PWL model in Thul and Coombes (2010), which is based on the established  $\text{Ca}^{2+}$  cycling model in Shiferaw et al. (2003). The PWL equations are given by

$$\begin{aligned} \frac{dc_s^\mu}{dt} &= \beta_s \left[ \frac{v_i}{v_s} \left( I_r^\mu - \frac{c_s^\mu - c_i^\mu}{\tau_s} - I_{\text{CaL}}^\mu \right) + I_{\text{NCX}}^\mu \right], \\ \frac{dc_i^\mu}{dt} &= \beta_i \left[ \frac{c_s^\mu - c_i^\mu}{\tau_s} - I_{\text{up}}^\mu \right] + \sum_{\eta} \frac{c_i^\eta - c_i^\mu}{\tau_c}, \\ \frac{dc_j^\mu}{dt} &= -I_r^\mu + I_{\text{up}}^\mu + \sum_{\eta} \frac{c_j^\eta - c_j^\mu}{\tau_{\text{sr}}}, \\ \frac{dc_u^\mu}{dt} &= \frac{c_j^\mu - c_u^\mu}{\tau_a}, \\ \frac{dI_r^\mu}{dt} &= -gI_{\text{CaL}}Q(c_u^\mu) - \frac{I_r^\mu}{\tau_r}. \end{aligned} \quad (1)$$

Here,  $c_s^\mu$ ,  $c_i^\mu$ ,  $c_j^\mu$ ,  $c_u^\mu$  and  $I_r^\mu$  denote the subsarcolemmal  $\text{Ca}^{2+}$  concentration, the bulk cytosolic  $\text{Ca}^{2+}$  concentration, the total  $\text{Ca}^{2+}$  concentration in the SR, the  $\text{Ca}^{2+}$  concentration in the unrecruited SR and the release current from the unrecruited SR into the subsarcolemmal space at the  $\mu$ th CRU, respectively.  $\beta_s$  and  $\beta_i$  denote buffer constants, and  $v_i$  and  $v_s$  refer to the volumes of the bulk and subsarcolemmal space, respectively. The  $\text{Ca}^{2+}$  flux through the L-type channel is given by  $I_{\text{CaL}}^\mu$  and that through the NCX by  $I_{\text{NCX}}^\mu$ .  $I_{\text{up}}^\mu$  denotes  $\text{Ca}^{2+}$  uptake through SERCA pumps.  $\tau_s$ ,  $\tau_c$ ,  $\tau_{\text{sr}}$ ,  $\tau_a$  and  $\tau_r$  represent time constants for transport between the subsarcolemmal space and the cytosolic bulk, cytosolic  $\text{Ca}^{2+}$  diffusion between adjacent CRUs, luminal  $\text{Ca}^{2+}$  diffusion between neighbouring CRUs, transport between the SR  $\text{Ca}^{2+}$  compartments and decay of the release current, respectively. The load-release function is given by  $Q$ , and  $g$  measures the release strength. Note that  $I_{\text{CaL}}$  is negative since it is an inward current, which renders the first term in the equation for  $I_r^\mu$  positive. The sum over  $\eta$  extends over nearest neighbours. For the full definition of the currents  $I_{\text{CaL}}^\mu$ ,  $I_{\text{NCX}}^\mu$  and  $I_{\text{up}}^\mu$  and the load-release function  $Q$ , we refer the reader to Thul and Coombes (2010). The clamped voltage for a pacing period  $T_p$  is

described by

$$V(t) = \begin{cases} V_+(t), & kT_p \leq t \leq (k+x)T_p, \\ V_{\min}, & (k+x)T_p \leq t < (k+1)T_p, \end{cases} \quad (2)$$

where  $k \in \mathbb{N}$  counts the number of APs and  $x = a_x/(a_x + T_p)$  with  $a_x = 2/3$ . Hence, the APD decreases with faster pacing periods. The resting potential is given by  $V_{\min} = -70\text{mV}$ , and  $V_+(t)$  captures the shape of the clamped voltage, given by

$$V_+(t) = V_{\min} + (V_{\max} - V_{\min}) \sqrt{1 - \left( \frac{t - kT_p}{xT_p} \right)^2}, \quad (3)$$

for  $kT_p \leq t \leq (k+x)T_p$ , where the maximal AP is given by  $V_{\max} = 30\text{mV}$ .

The PWL character of Eq. (1) results from a set of switches (Thul and Coombes, 2010), which are either state- or time-dependent. An example for a state-dependent switch is the change of the load release function when  $c_u^\mu$  crosses certain values, while the voltage-dependent inactivation of the L-type channel represents a time-dependent switch. The voltage dependence induces a time dependence since we clamp the voltage, i.e. it is a function of time only. Between switching events, Eq. (1) can be succinctly written as

$$\frac{dx}{dt} = Ax + F(t) + G \otimes Hx, \quad (4)$$

where  $x = (x_1, x_2, \dots, x_N)$  is a  $5N$  dimensional vector, where each entry  $x_\mu$ ,  $\mu = 1, \dots, N$ , corresponds the 5-dimensional state vector of a single CRU, i.e.  $x_\mu = (c_s^\mu, c_i^\mu, c_j^\mu, c_u^\mu, I_r^\mu)$ , in a network of  $N$  CRUs.  $F(t)$  is a  $5N$  dimensional vector that represents the voltage-dependence of the network and hence only depends on time.  $A \in \mathbb{R}^{5N \times 5N}$  is a constant matrix, and  $G \in \mathbb{N}^{N \times N}$  denotes the Laplacian matrix of the network. The matrix  $H \in \mathbb{R}^{5 \times 5}$  encodes through which variables the coupling occurs and what the coupling strength is. For instance, for cytosolic coupling only,  $H_{22} = 1/\tau_c$ , while all other components of  $H$  vanish. The usual tensor product is given by  $\otimes$ . We can then linearise Eq. (4) around the synchronous network state  $s(t)$  by making the ansatz  $x(t) = 1_N \otimes s(t) + \delta x$ , where  $1_N$  is an  $N$ -dimensional vector that only contains ones. Note that  $s(t)$  is 5-dimensional. Introducing the new variable  $\delta y = (\Gamma^{-1} \otimes I_{5 \times 5}) \delta x$ , where the columns of  $\Gamma$  contain the eigenvectors of  $G$  and  $I_{n \times n}$  is the  $n$ -dimensional identity matrix, it can be shown that the linearised system factorises into  $N$  5-dimensional equations (Pecora and Carroll, 1998). In other words, to determine linear stability, we do not need to investigate a  $5N$ -dimensional systems, but only  $N$  5-dimensional ones. Hence, we can write  $\delta y_{m+1} = S_m \delta y_0$ , i.e.

$$\delta y_{m+1} = \begin{pmatrix} \delta y_{m+1}^1 \\ \delta y_{m+1}^2 \\ \vdots \\ \delta y_{m+1}^N \end{pmatrix} = \begin{pmatrix} S_m^1 & 0 & \dots & \dots & 0 \\ 0 & S_m^2 & \ddots & \ddots & \vdots \\ \vdots & \ddots & \ddots & \ddots & \vdots \\ \vdots & \ddots & \ddots & S_m^{N-1} & 0 \\ 0 & \dots & \dots & 0 & S_m^N \end{pmatrix} \begin{pmatrix} \delta y_0^1 \\ \delta y_0^2 \\ \vdots \\ \delta y_0^N \end{pmatrix} \\ = S_m \delta y_0, \quad (5)$$

where  $S_m^i$  denotes the matrix for the  $i$ th 5-dimensional stability problem, and  $\delta y_0$  and  $\delta y_{m+1}$  represent the initial perturbation and the perturbation at the end of one pacing period, respectively. The index  $m$  indicates that there are  $m$  switches in Eq. (1). Let  $p_i$  denote an eigenvector of  $S_m$ . Then  $(\Gamma \otimes I_{5 \times 5})p$  are the eigenvectors that we plot in e.g. Fig. 4. From a conceptual point of view, the above method is similar to that developed in Li and Otani (2003) for a single CRU. In both cases, a matrix is computed that connects an initial perturbation to a final perturbation by fol-

lowing the flow of the underlying ODEs. The main difference is that this matrix can only be approximated in Li and Otani (2003), while we obtain an exact representation.

## Acknowledgement

This work was supported by the Engineering and Physical Sciences Research Council [grant number EP/P007031/1].

## Supplementary material

Supplementary material associated with this article can be found, in the online version, at doi:10.1016/j.jtbi.2019.06.016.

## References

- Aistrup, G.L., Shiferaw, Y., Kapur, S., Kadish, A.H., Wasserstrom, J.A., 2009. Mechanisms underlying the formation and dynamics of subcellular calcium alternans in the intact rat heart. *Circ. Res.* 104 (5), 639–649.
- Alvarez-Lacalle, E., Cantalapiedra, I.R., Peñaranda, A., Cinca, J., Hove-Madsen, L., Echebarria, B., 2013. Dependency of calcium alternans on ryanodine receptor refractoriness. *PLoS One* 8 (2), e55042.
- Alvarez-Lacalle, E., Echebarria, B., Spalding, J., Shiferaw, Y., 2015. Calcium alternans is due to an order-disorder phase transition in cardiac cells. *Phys. Rev. Lett.* 114 (10), 108101.
- Bers, D.M., 2002. Cardiac excitation-contraction coupling. *Nature* 415 (6868), 198–205.
- Bers, D.M., 2008. Calcium cycling and signaling in cardiac myocytes. *Annu. Rev. Physiol.* 70, 23–49.
- Bers, D.M., Shannon, T.R., 2013. Calcium movements inside the sarcoplasmic reticulum of cardiac myocytes. *J. Mol. Cell. Cardiol.* 58 (1), 59–66.
- Blatter, L.A., Kocksämper, J., Sheehan, K.A., Zima, A.V., Hüser, J., Lipsius, S.L., 2003. Local calcium gradients during excitation-contraction coupling and alternans in atrial myocytes. *J. Physiol.* 546 (Pt 1), 19–31.
- Cantalapiedra, I.R., Alvarez-Lacalle, E., Peñaranda, A., Echebarria, B., 2017. Minimal model for calcium alternans due to SR release refractoriness. *Chaos* 27 (9), 093928.
- Cherry, E.M., 2017. Distinguishing mechanisms for alternans in cardiac cells using constant-diastolic-interval pacing. *Chaos* 27 (9), 093902.
- Diaz, M.E., Eisner, D.A., O'Neill, S.C., 2002. Depressed ryanodine receptor activity increases variability and duration of the systolic  $\text{Ca}^{2+}$  transient in rat ventricular myocytes. *Circ. Res.* 91 (7), 585–593.
- Díaz, M.E., O'Neill, S.C., Eisner, D.A., 2004. Sarcoplasmic reticulum calcium content fluctuation is the key to cardiac alternans. *Circ. Res.* 94 (5), 650–656.
- Edwards, J.N., Blatter, L.A., 2014. Cardiac alternans and intracellular calcium cycling. *Clin. Exp. Pharmacol. Physiol.* 41 (7), 524–532.
- FitzHugh, R., 1961. Impulses and physiological states in theoretical models of nerve membrane. *Biophys. J.* 1 (6), 445–466.
- Gaeta, S.A., Bub, G., Abbott, G.W., Christini, D.J., 2009. Dynamical mechanism for subcellular alternans in cardiac myocytes. *Circ. Res.* 105 (4), 335–342.
- Gaeta, S.A., Christini, D.J., 2012. Non-Linear dynamics of cardiac alternans: subcellular to tissue-level mechanisms of arrhythmia. *Front. Physiol.* 3, 157.
- Gaeta, S.A., Krogh-Madsen, T., Christini, D.J., 2010. Feedback-control induced pattern formation in cardiac myocytes: a mathematical modeling study. *J. Theor. Biol.* 266 (3), 408–418.
- Groenendaal, W., Ortega, F.A., Krogh-Madsen, T., Christini, D.J., 2014. Voltage and calcium dynamics both underlie cellular alternans in cardiac myocytes. *Biophys. J.* 106 (10), 2222–2232.
- Huertas, M.A., Smith, G.D., Gyorke, S., 2010.  $\text{Ca}^{2+}$  alternans in a cardiac myocyte model that uses moment equations to represent heterogeneous junctional SR  $\text{Ca}^{2+}$ . *Biophys. J.* 99 (2), 377–387.
- Jordan, P.N., Christini, D.J., 2007. Characterizing the contribution of voltage- and calcium-dependent coupling to action potential stability: implications for repolarization alternans. *Am. J. Physiol. Heart Circ. Physiol.* 293 (4), H2109–18.
- Kanaporis, G., Blatter, L.A., 2017. Alternans in atria: mechanisms and clinical relevance. *Medicina (Kaunas, Lithuania)* 53 (3), 139–149.
- Kocksämper, J., Blatter, L.A., 2002. Subcellular  $\text{Ca}^{2+}$  alternans represents a novel mechanism for the generation of arrhythmogenic  $\text{Ca}^{2+}$  waves in cat atrial myocytes. *J. Physiol.* 545 (1), 65–79.
- Krogh-Madsen, T., Christini, D.J., 2012. Nonlinear dynamics in cardiology. *Annu. Rev. Biomed. Eng.* 14, 179–203.
- Li, M., Otani, N.F., 2003. Ion channel basis for alternans and memory in cardiac myocytes. *Ann. Biomed. Eng.* 31 (10), 1213–1230.
- Li, Y., Diaz, M.E., Eisner, D.A., O'Neill, S., 2009. The effects of membrane potential, SR  $\text{Ca}^{2+}$  content and RyR responsiveness on systolic  $\text{Ca}^{2+}$  alternans in rat ventricular myocytes. *J. Physiol.* 587 (Pt 6), 1283–1292.
- McKean, H.P., 1970. Nagumo's equation. *Adv. Math.* 4 (3), 209–223.
- Nagumo, J., Arimoto, S., Yoshizawa, S., 1962. An active pulse transmission line simulating nerve axon. In: *Proceedings of the IRE*, 50, pp. 2061–2070.

- Nivala, M., Qu, Z., 2012. Calcium alternans in a couplon network model of ventricular myocytes: role of sarcoplasmic reticulum load. *Am. J. Physiol. HeartCirc. Physiol.* 303 (3), H341–52.
- Pecora, L., Carroll, T., 1998. Master stability functions for synchronized coupled systems. *Phys. Rev. Lett.* 80 (10), 2109–2112.
- Picht, E., Zima, A.V., Shannon, T.R., Duncan, A.M., Blatter, L.A., Bers, D.M., 2011. Dynamic calcium movement inside cardiac sarcoplasmic reticulum during release. *Circ. Res.* 108 (7), 847–856.
- Qu, Z., Hu, G., Garfinkel, A., Weiss, J.N., 2014. Nonlinear and stochastic dynamics in the heart. *Phys. Rep.* 543 (2), 61–162.
- Qu, Z., Liu, M.B., Nivala, M., 2016. A unified theory of calcium alternans in ventricular myocytes. *Sci. Rep.* 6, 35625.
- Qu, Z., Nivala, M., Weiss, J.N., 2013. Calcium alternans in cardiac myocytes: order from disorder. *J. Mol. Cell. Cardiol.* 58, 100–109.
- Qu, Z., Xie, Y., Garfinkel, A., Weiss, J.N., 2010. T-wave alternans and arrhythmogenesis in cardiac diseases. *Front. Physiol.* 1, 154.
- Restrepo, J.G., Karma, A., 2009. Spatiotemporal intracellular calcium dynamics during cardiac alternans. *Chaos* 19 (3), 037115.
- Restrepo, J.G., Weiss, J.N., Karma, A., 2008. Calsequestrin-mediated mechanism for cellular calcium transient alternans. *Biophys. J.* 95 (8), 23–23.
- Rovetti, R., Cui, X., Garfinkel, A., Weiss, J.N., Qu, Z., 2010. Spark-induced sparks as a mechanism of intracellular calcium alternans in cardiac myocytes. *Circ. Res.* 106 (10), 1582–1591.
- Shiferaw, Y., Karma, A., 2006. Turing instability mediated by voltage and calcium diffusion in paced cardiac cells. *Proceedings of the National Academy of Sciences of the United States of America* 103 (15), 5670–5675.
- Shiferaw, Y., Sato, D., Karma, A., 2005. Coupled dynamics of voltage and calcium in paced cardiac cells. *Phys. Rev. E* 71 (2 Pt 1), 021903.
- Shiferaw, Y., Watanabe, M.A., Garfinkel, A., Weiss, J.N., Karma, A., 2003. Model of intracellular calcium cycling in ventricular myocytes. *Biophys. J.* 85 (6), 3666–3686.
- Shkryl, V.M., Maxwell, J.T., Domeier, T.L., Blatter, L.A., 2012. Refractoriness of sarcoplasmic reticulum  $Ca^{2+}$  release determines  $Ca^{2+}$  alternans in atrial myocytes. *Am. J. Physiol. HeartCirc. Physiol.* 302 (11), H2310–20.
- Swietach, P., Spitzer, K.W., Vaughan-Jones, R.D., 2008.  $Ca^{2+}$ -mobility in the sarcoplasmic reticulum of ventricular myocytes is low. *Biophys. J.* 95 (3), 1412–1427.
- Thul, R., Coombes, S., 2010. Understanding cardiac alternans: a piecewise linear modeling framework. *Chaos* 20 (4), 045102.
- Tian, Q., Kaestner, L., Lipp, P., 2012. Noise-free visualization of microscopic calcium signaling by pixel-wise fitting. *Circ. Res.* 111 (1), 17–27.
- Tomek, J., Tomková, M., Zhou, X., Bub, G., Rodriguez, B., 2018. Modulation of cardiac alternans by altered sarcoplasmic reticulum calcium release: a Simulation study. *Front. Physiol.* 9, 1306.
- Weiss, J.N., Karma, A., Shiferaw, Y., Chen, P.-S., Garfinkel, A., Qu, Z., 2006. From pulsus to pulseless: the saga of cardiac alternans. *Circ. Res.* 98 (10), 1244–1253.